Topological-Insulator Spin Transistor

Linh T. Dang,[1] Oliver Breunig,[1] Zhiwei Wang,[1,†] Henry F. Legg,[2] and Yoichi Ando[1,*]

[1] *Physics Institute II, University of Cologne, D-50937 Köln, Germany*

[2] *Department of Physics, University of Basel, CH-4056 Basel, Switzerland*

(Received 24 March 2023; revised 3 June 2023; accepted 2 August 2023; published 25 August 2023)

When a charge current is injected into the surface state of a topological insulator (TI), the resulting shift of the spin-momentum-locked Fermi surface leads to the appearance of a net spin polarization. The helical spin structure of the Dirac-cone surface state of a TI should lead to a fixed sign of this spin polarization for a given current direction, but experimentally both signs that agree and disagree with the theory expectation for the surface state Dirac cone have been observed in the past. Although the origin of the wrong sign has not been conclusively elucidated, this observation points to the possibility that one may switch the spin polarization at will to realize a spin transistor operation. Here we report the observation of both signs of spin polarization in the very same device and demonstrate the tunability between the two by electrostatic gating, which gives a proof of principle of a TI spin transistor. This switching behavior is explained using a minimal model of competing contributions from the topological surface state and trivial Rashba-split states.

DOI: 10.1103/PhysRevApplied.20.024065

I. INTRODUCTION

A Datta-Das spin transistor [1] can be an energy-efficient alternative to the traditional transistor and represents one of the crucial components in spintronics [2,3]. Instead of tuning the carrier density in a traditional field-effect transistor, in a spin transistor the gate acts on the spin degree of freedom of electrons. The main component of a Datta-Das spin transistor is a material with strong Rashba spin-orbit coupling [1]. Significant efforts have been devoted to realize this type of spin transistor [4,5], most notably on a gated two-dimensional (2D) electron gas [4,6]. In this context, topological insulators (TIs) arise as a promising class of materials for spintronics [7–18] due to the helical spin-momentum locking in their surface state [19], and spin transistors would be an interesting application of TIs [14,20].

When a charge current is injected into the surface state of a TI, the resulting shift of the Fermi surface leads to a net spin imbalance in the current-carrying electrons, which is called the Edelstein effect [21]. Historically, while Edelstein discussed this effect [21] for Rashba-type spin-orbit coupling that is relevant in the TI context, a similar effect was discussed by Aronov *et al.* [22,23] for Dresselhaus-type spin-orbit coupling. Irrespective of its origin, this allows for generating a spin-polarized current without the need for a ferromagnetic (FM) spin source. In the past, multiple methods for the detection of this current-induced spin polarization (CISP) have been proposed and experimentally realized [7,24–27]. Among these methods, using a FM potentiometer to probe the spin polarization as a spin voltage [28] is convenient, as it enables simple electrical detection of the gate-induced sign change of the CISP, which is the key signature of the spin transistor operation presented in this paper.

In the topological surface state (TSS) of TIs, the helicity of the spin polarization changes sign across the Dirac point (DP) [19]. Hence, at first sight, one might expect that tuning the chemical potential across the DP by electrostatic gating can easily reverse the surface spin polarization in a current-biased TI. However, the Fermi velocity of the surface electrons also changes sign at the DP, which results in the same spin polarization for the same direction of the applied current. This mechanism has been explained in detail by Yang *et al.* [14]. In other words, in TIs, the helicity of their TSS allows only one type of spin polarization that is determined by the sign of the applied current. Indeed, the expected sign of the CISP has been observed in many experiments [8,9,11–16].

However, the opposite sign of the CISP has also been reported in TI devices [7,14,29], and this must be explained by a different physical mechanism than the current-carrying TSS electrons. The origin of this anomalous CISP has been a topic of interest and several possible explanations have been proposed, including the bulk spin Hall effect [29], Rashba-split and other spin-orbit-split

*ando@ph2.uni-koeln.de

†Present address: School of Physics, Beijing Institute of Technology, Beijing 100081, China.

states [14,30,31], and spin-dependent interface resistance [32]. Unfortunately, no decisive evidence of any of these explanations has been found experimentally, leaving the origin of the opposite CISP ambiguous. Nevertheless, it has been remarked that devices with a higher carrier density (and hence a higher chemical potential) tend to exhibit the unexpected CISP [14,29]. Regardless of its origin, the existence of the CISP of opposite sign in devices with a higher chemical potential suggests that it may be possible to control the sign of the CISP with electrostatic gating, thus realizing a spin transistor operation in a TI [14]. So far, while a gate tunability of the amplitude of the CISP (showing a peak near the DP) has been reported [13], the gate-induced switching of the CISP has not been achieved [13,29]; different signs of the CISP have been observed only in different devices [14,29].

Note that the spin transistor operation of this type relies on the Edelstein effect and thus occurs in the diffusive transport regime. This is in contrast to the Datta-Das spin transistor, which works mainly in the ballistic transport regime [33]. Therefore, Zitterbewegung and/or the side-jump effect, which may lead to a gate-dependent CISP in the ballistic regime [34,35], are not relevant in the present case. More detailed discussions on the difference between the present TI spin transistor and the Datta-Das device are given in the Appendix. In passing, we note that the roles of side-jump and skew-scattering effects in the diffusive and ballistic transport regime are an interesting subject in their own right [34,36] and their understanding may have implications for future spin transistors.

For the purpose of controlling the sign of the spin voltage with electrostatic gating, in contrast to a previous study [14] that used thick TI flakes, in this work we base our devices on TI flakes that were exfoliated to the thicknesses between 10 and 20 nm in order to achieve a sizeable tunability of the top TSS from bottom gating, while avoiding hybridization of the top and bottom surface states that occurs in even thinner TIs [37]. Secondly, we used bulk crystals of $Bi_{2-x}Sb_xTe_{3-y}Se_y$ (BSTS) with different compositions to obtain different chemical potentials at zero gate voltage. Upon gating, we observed a maximum in the CISP near the DP in one device and sign switching of the CISP, with complicated multiple-switching behavior, in two other devices. Furthermore, we provide a theoretical explanation of this switching behavior based on the assumption that the opposite sign of the CISP originates from trivial Rashba-split states on the surface of a TI.

II. EXPERIMENTAL RESULTS

A. Devices for spin voltage detection

For all of the devices analyzed, the voltage V_S measured between the permalloy (Py) lead and its reference lead, which reflects the relative orientations of the spins in Py and in the TI surface, shows a clean hysteresis as a function of $B_\parallel$ with a coercive field of about 20 Oe as expected for a thin ($\sim$ 30 nm) Py strip that is magnetized along its easy axis [see Fig. 1(a) for device schematics]. In contrast to previous experiments where averaging of multiple sweeps was required to extract the hysteresis [8,14], here we could resolve it even from a single magnetic field sweep due to an enhanced signal-to-noise ratio and reduced charge fluctuations. The latter is due to a better tunnel barrier made of SiN_x (see Appendix 3). The size of the voltage hysteresis (i.e., the spin voltage ΔV_S which is proportional to the CISP on the TI surface) shows an approximately linear dependence on the applied current [Fig. 1(b)] and changes sign upon reversal of the current direction, as expected. The spin resistance $R_S = \Delta V_S/I_{dc} = 1.18\ \Omega$ in device A is similar to previously reported values in the range of 1–5 Ω [11,16,32].

Next, we turn to the dependence of the spin voltage on the chemical potential (gate voltage) to study the different signs that have been reported. Here, for the first time we observed both signs of the spin voltage in a single device upon changing the gate voltage [Figs. 2(f) and 2(g)]. However, before discussing the devices presenting the sign reversal, we first consider the reference device A [Fig. 2(a)]. The TI flake used for device A was bulk-insulating and the chemical potential can be tuned to the DP with a gate voltage $V^{\rho}_{G,peak} \approx -75$ V, as reflected in a resistance peak of the longitudinal resistivity ρ. Similarly, ΔV_S also presents a maximum, but at a slightly different gate voltage $V^{S}_{G,peak} \approx -60$ V [Fig. 2(c)]. Even though ΔV_S is expected to be maximum when the chemical potential is at the DP [13], a finite difference between $V^{\rho}_{G,peak}$ and $V^{S}_{G,peak}$ may originate from the fact that both the top and bottom TSSs contribute to the resistance of the flake, while only the top TSS contributes to the spin voltage. These two TSSs experience different chemical potential tuning by the gate. Tuning the gate away from the spin voltage peak, ΔV_S decays quickly and saturates for $V_G \gtrsim -30$ V, which fits well with the expectation for a single Dirac cone contribution to spin polarization [27,38]. From an estimation of the geometric capacitance of the gate for this device, the conduction band edge is expected to be reached at a gate voltage $V_{CB} \approx 60$ V. Since the Rashba-split band is formed very close to the conduction band edge, one expects the onset of its contribution at this voltage. The absence of clear features in ΔV_S around 60 V is explained by screening effects or by an electric-field-induced suppression of the Rashba splitting due to the large gate voltage that is required to tune to the conduction band (see below for details).

B. Gate-controlled sign reversal of the spin voltage

To better access the Rashba-split band, another device B was fabricated from a more *n*-type TI flake, such that a

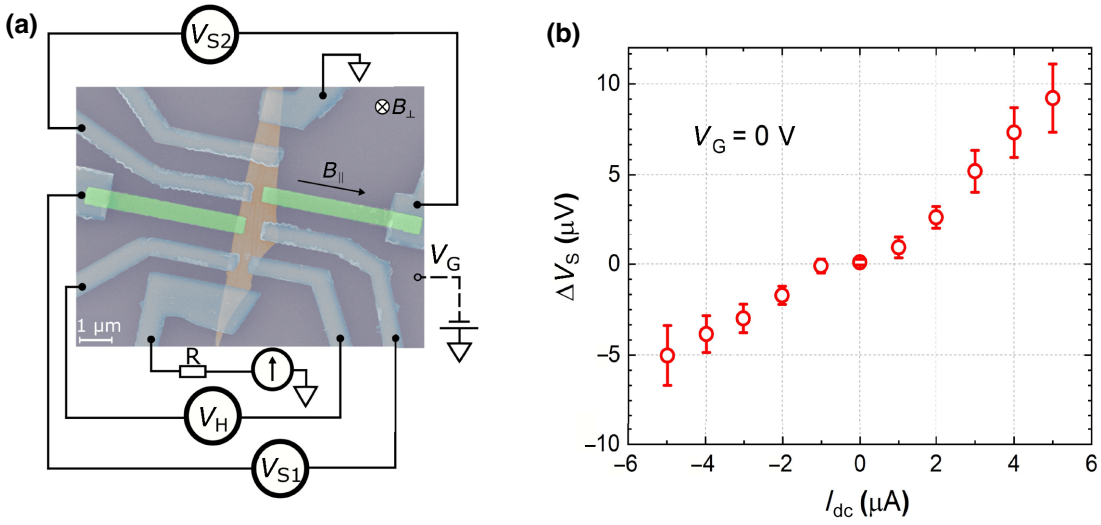

FIG. 1. Topological-insulator (TI) spin transistor device. (a) False-colored scanning electron microscope image of device A with the measurement scheme. Normal contacts are fabricated using Nb (shaded in light blue). The tunnel barrier between the permalloy (Py) leads (light green) and the BSTS flake (light orange) is formed by a layer of SiN_x deposited right after exfoliation of the flake. A direct current I_{dc} is injected from the bottom Nb lead via a 1-MΩ resistor and drained at the top Nb lead. The voltages between the neighboring Nb and Py leads, V_{S1} and V_{S2}, as well as the Hall voltage V_H are acquired while sweeping the magnetic field $B_\parallel$ aligned along the long axis of the Py leads, leading to an in-plane magnetization M_{FM} of the Py leads. An out-of-plane magnetic field $B_\perp$ was applied for Hall measurements. The gate voltage V_G is applied to the back side of the degenerately doped Si substrate which is covered by 290 nm of SiO_2 acting as a gate dielectric. (b) The spin voltage ΔV_S (open symbols) shows an approximately linear dependence on the applied current I_{dc} and its sign inverts upon reversal of the current direction. The data shown were measured on device A at $V_G = 0$ V.

smaller gate voltage suffices to tune the chemical potential to the conduction band. In this device, the spin voltage indeed shows a much richer gate response [Fig. 2(d)]. The V_G dependence of ρ in this device [Fig. 2(b)] shows n-type behavior with smaller absolute values of ρ and a reduced gate tunability, both indicating that the chemical potential in this device without gating is closer to the conduction band. Comparing the resistivity values of this device to device A, a rough estimate of a gate voltage shift between devices A and B of about 50 V can be deduced. Consistent with this estimate, the resistance cannot be tuned to a peak within the gate voltage range accessible in our experiment and the device remains n-type. Interestingly, the spin voltage ΔV_S of device B shows multiple sign switches (later we show that the positive and negative sign of ΔV_S can be attributed to the TSS and the trivial Rashba bands, respectively). At large negative gate voltages, the positive sign is consistent with a dominant TSS contribution. Upon sweeping V_G in the positive direction, however, ΔV_S drops abruptly near -70 V and a sign reversal occurs close to -50 V, indicating the appearance of another contribution and eventual reversal of the spin polarization. With further sweeping of V_G in the positive direction, the sign of ΔV_S switches a couple of times and eventually converges to a negative value at $V_G \gtrsim 40$ V. Even though ΔV_S seemingly fluctuates between plus and minus, it should be noted that for a given fixed gate voltage, the hysteresis loops such as shown in Figs. 2(f) and 2(g) are static and reproducible. Yet, their sign can invert quickly with a small change in the gate voltage. In other words, the V_G dependence of ΔV_S reflects an intrinsic property that changes rapidly within a certain gate-voltage range and it is not the result of a random fluctuation or instability. Here, the opposite spin polarization was observed at different gate voltages in the same device, which has not been reported before in this type of TI-based devices.

Notably, the spin voltage reversal was observed in the more n-type device B, while it was completely absent in device A. The absence of Rashba contributions upon gating in device A could be explained in two ways. First, due to the screening effect from the FM lead, the chemical potential underneath the lead is not efficiently tuned by the electrostatic gate. Therefore, even at a gate voltage high enough to bring a crystal of similar pristine carrier density to the conduction band, the chemical potential in device A may still reside in the bulk gap. Second, it is known that a strong electric field can affect the splitting of a Rashba-split state [39], effectively changing (or even reversing) its contribution to the spin polarization. In device A, the chemical potential is closer to the DP without gating, hence a larger gate voltage (i.e., a large electric field) is required to bring the chemical potential to the conduction band edge. This large electric field can then weaken the contribution from the Rashba band to the spin polarization,

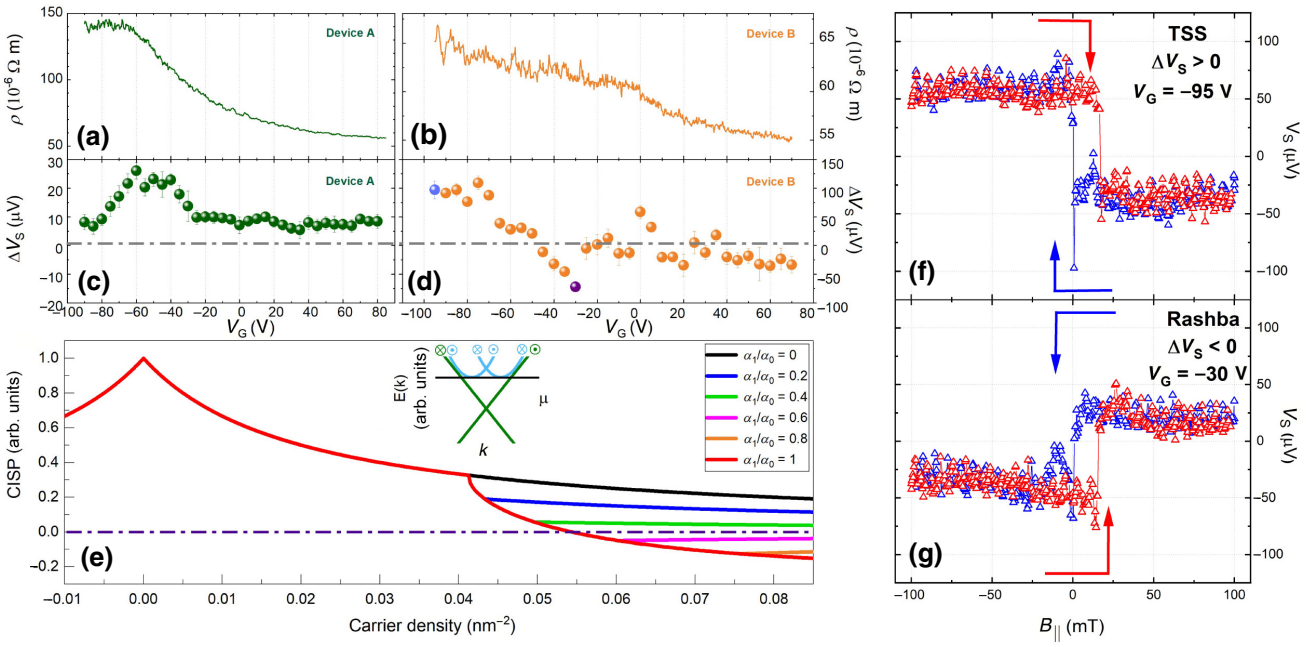

FIG. 2. Gate-controlled spin voltage. (a),(b) Resistivity ρ as a function of gate voltage V_G for device A and B, respectively, measured in a four-terminal configuration. (c),(d) Spin voltage ΔV_S as a function of V_G in device A and B, respectively. In device B, multiple sign changes are observed. The dash-dotted gray line denotes zero spin voltage for both devices. (e) Theoretically calculated carrier-density dependence of the current-induced spin polarization (CISP) for various ratios of the contributions from a single Rashba band and the topological surface state (TSS), α_1/α_0. The CISP has a global peak at the Dirac point (DP) and an abrupt change when the chemical potential reaches the Rashba band. With $\alpha_1/\alpha_0 > 0.4$, the total CISP can turn negative (zero marked by the dash-dotted line). The parameters used are $\alpha_0 = 250$ meV nm (which is consistent with $v_F \approx 4 \times 10^5$ m/s of the TSS), $m_1 = 300$ meV nm^2 (which gives a v_F similar to that of the TSS) and $\mu_1 = 180$ meV (close to the bulk conduction band edge); the behavior of the CISP is, however, only weakly dependent on the exact choice of parameters. The complicated multiple changes of sign of the CISP observed experimentally can be understood by the presence of multiple Rashba bands and, for instance, modification of the Rashba strength α by the electric field from the gate. Inset: Schematics of a TSS (green) with a Rashba band (blue) at about 200 meV away from the DP. The momentum-locked spin of electrons in each branch is denoted on top. The chemical potential (black line) crossing the Rashba band bottom corresponds to the kink in the CISP at a carrier density of about 0.04 nm^{-2}. (f),(g) Examples of the raw data of the hysteresis observed in the V_S vs $B_{||}$ behavior at V_G of −95 and −30 V; the corresponding ΔV_S values extracted from these data are shown in panel (d) with blue and purple symbols, respectively.

leading to the absence of an opposite spin polarization in device A. Both mechanisms can be circumvented by employing a crystal with a higher pristine chemical potential. Indeed, device B as well as device C, which were fabricated from such a crystal (see Appendix), exhibit the Rashba-type contribution (i.e., the sign reversal of ΔV_S).

C. Effects of chemical potential pinning by Py and spin diffusion

One of the previous explanations of the unexpected sign of the spin voltage was based on the contribution of the trivial Rashba-split states formed underneath the metallic FM contacts due to band bending [14]. However, in this scenario one would expect that the chemical potential underneath the metal contacts (i.e., the spin detector) is fixed and cannot be changed with the gate. Thus, at first sight, one might not expect any gate dependence of the spin voltage from this area at all. However, our data clearly show that the spin voltage detected is gate-tunable: device A exhibits a peak in ΔV_S near the DP, indicating that the chemical potential of the spin-polarized electrons is indeed modified and can be brought to the DP. If the CISP originated from electrons underneath the FM leads alone, this should not happen. This contradiction may be resolved by considering spin diffusion from the (free) area not covered by the FM leads to the area underneath the FM leads. These two areas differ in terms of the electronic states and the gate tunability: in the free area, the chemical potential is not pinned, but can be tuned by the bottom gate via the electrostatic coupling between the top and bottom TSSs [40]. In addition, Rashba-split states due to trivial surface states can be formed in the free area [41–44]. Those may become visible in the CISP probed by the FM detector via spin diffusion. In the area beneath the FM lead, Rashba-split states would also exist due to band bending effects at the Py-TI interface and, even though the chemical potential is pinned here, the size of the Rashba

splitting is modified by the electric field generated upon gating, leading to a modification of the CISP in this area as well [14,39]. It would be interesting to further elucidate the appearance of the trivial Rashba states using the quantum capacitance measurements [45], which can probe the gate-voltage dependence of the surface density of states.

The spin voltage detected in the experiment reflects all of these sources of spin polarization via averaging the CISP in an area that is larger than the detector by an area set by the order of the spin diffusion length. Typical spin diffusion lengths in TI materials (up to 1 μm, [46]) are of similar order to the size of the present FM detector, such that the observed CISP can be understood as simply the average of the contributions from the two areas.

III. THEORETICAL UNDERSTANDING OF THE SPIN TRANSISTOR EFFECT

The mechanism of the spin transistor effect is graphically demonstrated in Fig. 3(d), which depicts the different behaviors of devices A and B. In device A, for bringing the chemical potential into the Rashba states of the free area, a very large gate voltage is required, which significantly reduces the Rashba coefficient such that there is no sizeable contribution of Rashba type to the detected CISP. Additionally, the Rashba states formed underneath the FM may contribute as well, but the magnitude is mostly set by the details of the FM-TI interface and the tunability by the gate is limited. In the more *n*-type device B (and in device C; see Appendix) the Rashba splitting in the free area remains large enough upon gate tuning to induce a negative contribution to the CISP.

The key features of the CISP observed in our experiment can be described with a minimal model that includes the contributions from both the topological surface state and surface Rashba states. We consider a simple Hamiltonian for the surface of our TI, such that

$$H = \sum_i \tau_i \left[\frac{\mathbf{k}^2}{2m_i} + \alpha_i(\sigma_y k_x - \sigma_x k_y) - \varepsilon_i - \mu \right], \quad (1)$$

here σ_x and σ_y are Pauli matrices in spin space, τ_i is a diagonal matrix in band space that distinguishes the ith band, m_i is the effective mass of this band, ε_i governs the $k = 0$ crossing point of this band, and μ is the chemical potential. In particular, we label the topological surface state by $i = 0$ such that $m_0^{-1} = 0$ and measure the chemical potential from the Dirac point such that $\varepsilon_0 = 0$. Note that throughout we set $\hbar = 1$. Importantly, we set the α_i parameters of this model all of the same sign, such that the Rashba parameters of the trivial surface states are consistent with the sign of the helicity of the topological surface state (see Fig. 3).

Within this simple model, the CISP due to an electric field $\mathcal{E}_x$ can be written as [16] (see Appendix for full details)

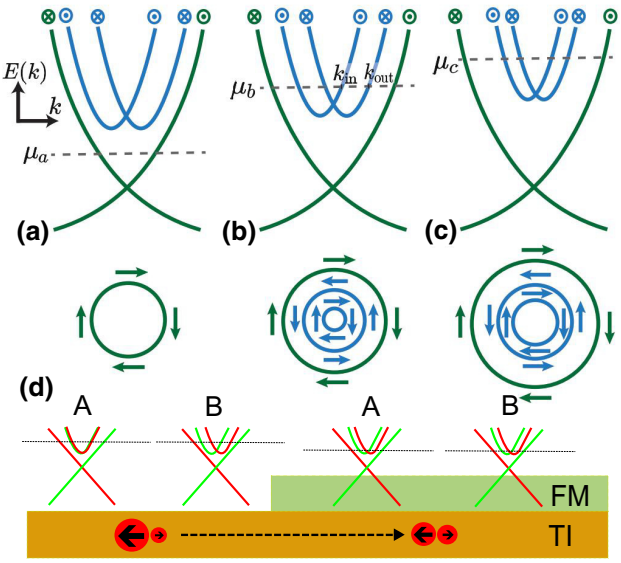

FIG. 3. Schematics of the surface bands during gating. (a) When the chemical potential is located close to the Dirac point, the CISP arises solely from the TSS. (b) As the chemical potential is raised close to the bulk conduction band, trivial Rashba surface bands contribute to the CISP; here, only a single band is shown. The contribution of trivial bands has opposite sign to the TSS contribution and can cause a sign change in the total CISP. (c) As the chemical potential is tuned to a higher value, the contribution of the Rashba band can be further modified; this could occur, for example, due to the electric field generated by gating (shown) or the momentum dependence of the Rashba coefficient α_i (not shown). As a result, the CISP can change sign depending on the relative values of the trivial and topological CISP contributions; if there are multiple Rashba bands, the sign change can occur multiple times. (d) Two parts of the device: free TI surface, left, and the surface covered by the FM lead (green), right. The band structures of these two parts are sketched on top of them. Both of them have spin-polarized (red and green) bands: TSS and Rashba-split states. The chemical potentials and the Rashba splittings are different between the two areas, resulting in different CISPs (red circles with arrows denote the spin direction). Electrons with different spin polarization then diffuse from one part to another. The sketch is for a finite gate voltage applied, which has tuned the chemical potential into the Rashba bands on the left, while it is pinned on the right side. Labels A and B refer to the scenarios in devices A and B. Note the different sizes of the Rashba splitting between devices A and B in the free area.

$$P_{\mathrm{CI}} = \frac{n_\uparrow - n_\downarrow}{n} = e\mathcal{E}_x \frac{\sum_i \Delta_i}{4\pi n}, \quad (2)$$

where $n_\uparrow$ $n_\downarrow$ is the spin-up (spin-down) density and $n = n_\uparrow + n_\downarrow$ is the total density. The contribution from the topological surface state ($i = 0$) is

$$\Delta_0 = \tau_0 k_{F,0} \approx \frac{8\pi\alpha_0}{\gamma}, \quad (3)$$

where γ is the impurity strength. Similarly, the contributions of the Rashba surface states ($i \geq 1$) are of opposite sign and take the form

$$\Delta_i = -\tau_i \left(k_{F,i}^{\text{out}} - k_{F,i}^{\text{in}}\right) \approx -\frac{8\pi}{m_i \gamma} \left(k_{F,i}^{\text{out}} - k_{F,i}^{\text{in}}\right), \quad (4)$$

where $k_{F,i}^{\text{out}}$ ($k_{F,i}^{\text{in}}$) are the outer (inner) Fermi-momenta of the ith Rashba surface band (see Fig. 3). We also defined the scattering time for each band, τ_i, and in the approximation we assume that only intraband scattering is relevant, such that τ_i is governed by the impurity strength, γ, and the density of states of the band i.

First we show how a single change of sign of the CISP can be understood by a model including the interplay of the TSS and a single pair of Rashba spin-split bands with fixed parameters, as in Fig. 2(e). The evolution of the bands, including the effects of increasing gate-induced electric field, is depicted in Figs. 3(a)–3(c). When the chemical potential is in the vicinity of the Dirac point [Fig. 3(a)], the CISP is entirely dominated by the contribution of the TSS. However, when the chemical potential is tuned close to the edge of the bulk conduction band [see Fig. 3(b)] the trivial Rashba surface states result in a contribution to the CISP which has the opposite sign and can cause a total sign change of the CISP if $\Delta_1 > \Delta_0$.

We now comment on how the full experimental behavior, including multiple CISP sign changes far from the Dirac point, can be understood within the simple model of Eq. (1). The key to this behavior is the presence of multiple Rashba bands, which has been elucidated for a doped TI surface [41–44]. The CISP contribution from each of them, $\Delta_{i>0}$, can be dependent on the chemical potential and the gate voltage. Such a dependence is natural because, for instance, the Rashba strength α_i will be modified by the electric field that arises due to gating [39] [see Fig. 3(c)] and/or the coefficient α_i will have a dependence on momentum k. Furthermore, the mass m_i will have momentum dependent corrections that could also reduce the magnitude of Δ_i for the Rashba bands and the scattering time τ_i can also be dependent on the chemical potential. In contrast, it is known that the Fermi velocity, α_0, of the topological surface Dirac cone increases close to the bulk conduction band [19], and this will lead to a corresponding increase in the contribution Δ_0 [see Eq. (3)]. Hence, the experimentally observed multiple switches can be qualitatively explained by the variations of the relative magnitudes of the topological ($\Delta_{i=0}$) and trivial CISP contributions ($\Delta_{i>0}$), when the latter stems from more than one Rashba band. The detailed understanding of the complicated multiple switchings behavior is an important subject for the future applications of TI spin transistors.

It is prudent to mention that the magnetic proximity effect (MPE) can cause a gate-voltage-controlled sign reversal of the spin polarization in graphene [47], as experimentally observed when the ferromagnet is made to have only a 1D contact to the edge of the graphene, such that the chemical potential of the graphene bulk is not pinned by the ferromagnet [48]. In our experiment, the Py lead has a 2D contact to the TI surface to cause a chemical-potential pinning, and hence the MPE is not likely to be relevant to the gate-voltage-controlled sign reversal of the spin polarization observed here. Nevertheless, the MPE on the TI surface was predicted to give rise to various spintronic functionalities, including spin valve and amplification [49]. Also, it was predicted that the tunneling anisotropic magnetoresistance caused by the MPE can be used for judging whether the spin-polarized current is mainly flowing through the topological surface states or through the trivial Rashba surface states [50].

We further mention that the physics of spin injection and detection is more complicated than a simple picture of linear impedance matching [2], and a clever use of the MPE enables the detection of a spin signal without a tunnel barrier in a graphene-based spintronic device [51].

IV. CONCLUSION

We studied the gate-voltage dependence of CISP in multiple devices fabricated from $Bi_{2-x}Sb_xTe_{3-y}Se_y$ crystals. We observed gate-controlled sign reversals of the CISP for the first time in TI devices, and such sign reversals were found to occur only in devices fabricated from n-type crystals. We argued that trivial Rashba-split states on the TI surface contribute to CISP with the opposite sign compared to that from the TSS, which enables a change of sign of the CISP. The existence of multiple Rashba bands [41–44] and the dependence of the Rashba parameter α on the electric field generated by the back gate [39], among others, play a crucial role in the competition between these two contributions to the CISP and likely cause the complicated multiple sign reversals in the experimentally observed CISP as a function of the gate voltage. Our devices demonstrate the feasibility of the spin transistor conceived by Yang *et al.* [14], while presenting the importance of spin diffusion in its working principle. The spin transistor effect demonstrated here will significantly widen the prospects of TIs for spintronic applications. For fundamental research, the miniaturization of the spin transistor into the ballistic transport regime would be extremely interesting, because the efficiency of the CISP would be drastically enhanced compared to the diffusive transport regime [19].

ACKNOWLEDGMENTS

This work has received funding from the Deutsche Forschungsgemeinschaft (DFG, German Research Foundation) under CRC 1238-277146847 (subprojects A04 and B01) and under 398945897, as well as under Germany's

Excellence Strategy – Cluster of Excellence Matter and Light for Quantum Computing (ML4Q) EXC 2004/1-390534769. H. F. Legg acknowledges support by the Georg H. Endress Foundation.

APPENDIX

1. Device fabrication

The data shown in this paper were taken from three different devices A, B, and C. Two different TI crystals were used for device fabrication: device A was fabricated from $BiSbTeSe_2$ bulk crystal, while devices B and C were fabricated from $Bi_{1.5}Sb_{0.5}Te_{1.3}Se_{1.7}$ crystal with a chemical potential closer to conduction band edge compared to the former. Both single crystals were grown by the modified Bridgman method. TI flakes were exfoliated from single crystals using standard scotch tape technique onto degenerately doped Si substrates coated by a 290-nm layer of SiO_2 acting as a gate dielectric. Thin flakes (of thickness less than 20 nm) with a suitable shapes and sizes and flat surfaces were selected using optical microscopy. After exfoliation the substrate was immediately loaded on to the vacuum chamber of the hot-wire chemical vapor deposition (HW CVD) machine to minimize any native oxide formation on the TI surface. There, a 1-nm-thick layer of SiN_x was deposited on top of the TI, acting as a capping layer and tunnel barrier at the same time. During the SiN_x deposition, the substrate temperature was observed to stay below 100 °C. Diluted ZEP 520A resist was spin-coated immediately after the SiN_x deposition. Electron beam lithography was performed using a Raith Pioneer Two system. Contacts were fabricated using niobium (Nb) and permalloy (Py) for the normal and FM contacts, respectively, by a liftoff technique. For normal leads, first the SiN_x layer was removed using reactive ion etching in CF_4 plasma, followed by the deposition of 35-nm-thick Nb via magnetron sputtering. In a second lithography, 30-nm-thick Py leads were deposited by thermal evaporation without removing the SiN_x layer. The tunnel-barrier resistances of the measured FM leads of devices A, B, and C were 4.2, 4.1, and 6.4 kΩ, respectively. Finally, 40-nm-thick Nb leads were fabricated to connect to prepatterned Au bonding pads.

2. Device summary

A total of nine batches with a SiN_x tunnel barrier were fabricated (each batch was a set of tens of devices fabricated on the same Si/SiO_2 chip, going through the same fabrication process). Different batches of fabrications were performed to optimize the SiN_x tunnel barrier for a suitable tunnel resistance, which we obtained in two of these batches. From the batches with optimized SiN_x fabrication, we measured 12 devices and the spin voltage was observed in three of them: device A came from a batch using $BiSbTeSe_2$ crystal, while devices B and C came from another batch using $Bi_{1.5}Sb_{0.5}Te_{1.3}Se_{1.7}$ crystal.

3. Measurements

All measurements were performed in an Oxford Instruments TRITON 200 dilution refrigerator at a base temperature of 20–40 mK. A vector magnet was used to allow measurement of multiple devices with different orientations in the same run. The wiring scheme of the spin voltage measurement is illustrated in Fig. 1(a). Direct current is applied using the two outer Nb contacts and an in-plane magnetic field $|B_\parallel| \leq 100$ mT is applied along the easy axis of the FM contact to switch its magnetization. The voltage V_S is measured between a FM lead and the opposing Nb lead as a function of the magnetic field using a Keithley 2182A nanovoltmeter; this contact arrangement minimizes the contribution of the longitudinal resistance. Further data treatments to subtract the remaining longitudinal resistance contribution are described below. The back-gate voltage is applied to the sample using a Keithley 2450 sourcemeter. Each measurement includes multiple forward (negative $B_\parallel$ to positive $B_\parallel$) and backward (positive $B_\parallel$ to negative $B_\parallel$) magnetic field scans. An average ΔV_S is deduced from multiple scans for each biased current or gate voltage to reduce the noise. The longitudinal resistance was measured in a standard four-probe configuration with a low-frequency (13.77 Hz) ac technique using a NF LI5640 lock-in amplifier.

4. Estimation of spin voltage

For each data point in the plots of ΔV_S vs V_G, the bottom gate voltage V_G is first set at the targeted value, then a bias current of 5 μA is applied through the device, followed by a magnetic field sweep applied perpendicular to the current direction. The magnetic field is first ramped up to B_{max}, then swept between $\pm B_{max}$ five times (once for device A) before being ramped back to zero. Each of these five down-up scans is then analyzed to extract ΔV_S. However, sometimes a sudden, irreproducible jump in the signal occurred during the scan, whose origin is unclear; such a random jump typically happened in one or two of the five scans recorded for each V_G, such that there were usually a sufficient number of scans at each V_G to extract ΔV_S without being affected by a random jump in the signal. Figure 4 demonstrates two scans, with and without a random jump. Among the five scans at each V_G, only those scans in which the random jumps in the signal do not hinder the determination of a stable high-field value of V_S were analyzed. Prior to the estimation of ΔV_S, a linear background subtraction process is performed on each gate-voltage scan set. Due to fabrication mismatch between the Py lead and its Nb counterpart, V_S always contains a small longitudinal ohmic voltage drop. This ohmic contribution

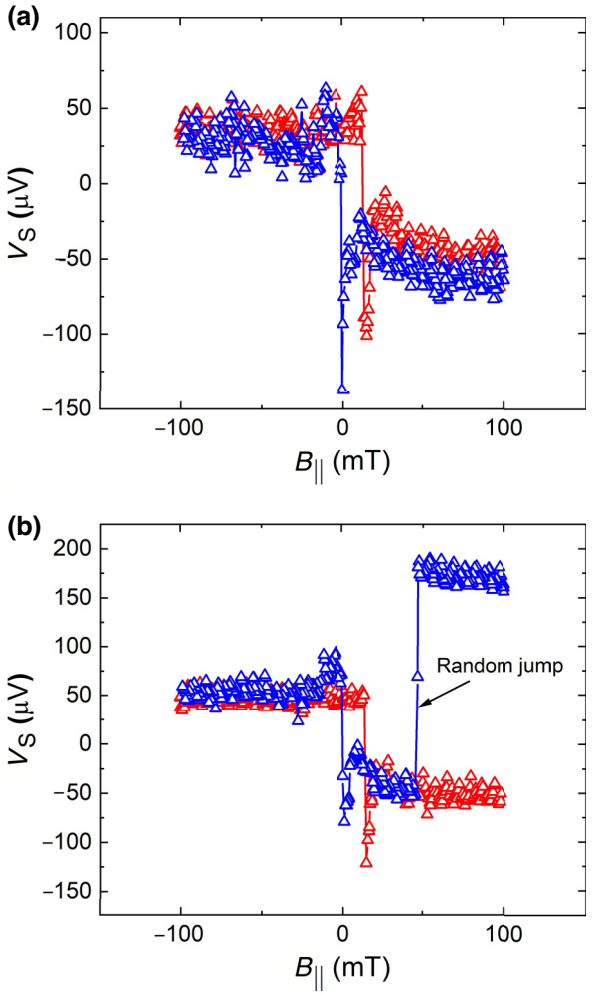

FIG. 4. (a) Scan without a random jump in the signal. (b) A random jump in the signal observed during the magnetic field scans in the same measurement setting. Multiple scans are performed for each V_G.

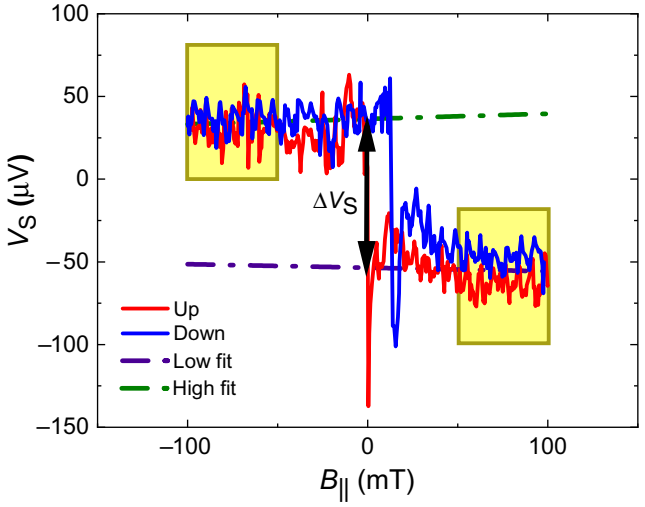

FIG. 5. Analysis of the data to extract the spin voltage. The light yellow box denotes the data range for fitting. The green and purple dash-dotted lines are the fitted lines for high and low potential, respectively. The spin voltage ΔV_S is the difference in the intersections of these lines on the V_S axis at $B_{||} = 0$ T.

can have a magnetic field dependence (due to the magnetoresistance of TI) and create spurious features in the measured voltage. In order to remove this contribution, a longitudinal voltage V_L was measured between two Nb leads (e.g., the two outer Nb leads in Fig. 1) during the magnetic field scan. This V_L was then normalized by the zero-field value: $V_{L(\text{norm})} = V_L/V_{L(B_{||}=0)}$. This normalized change of the longitudinal voltage was subtracted from V_S to obtain the background-subtracted V'_S as follows:

$$V'_S = V_S - V_{L(\text{norm})} \times V_{S(B_{||}=0)}. \tag{A1}$$

Afterwards, in order to extract ΔV_S from a single scan, we used linear fitting of the measured voltage as a function of applied magnetic field at large magnetic field ranges (near $\pm B_{\max}$). The exact fitting range depends on the behavior of the measured signal at each gate voltage. A linear fit which takes into account all data points from both up-sweep and down-sweep scans in the respective fitting range (large positive and negative $B_{||}$) is then performed. The fits give two linear curves, $V'_S = a_{1(2)}B_{||} + b_{1(2)}$, where the subscripts 1 and 2 denote whether the coefficients a and b belong to the large positive or the large negative fitting range, respectively. The difference in the intersections of these two linear fits on the V_S axis gives ΔV_S: namely, $\Delta V_S \equiv b_1 - b_2$. The sign of ΔV_S reflects its origin (positive for TSS, negative for Rashba). The error in b_1 (b_2) is defined as three times its standard deviation σ_1 (σ_2) in the fit. Hence, the error in ΔV_S is specified as $\epsilon_{\Delta V_S} = 3(\sigma_1 + \sigma_2)$. The process is illustrated in Fig. 5.

It is also important to note that a clear hysteretic voltage was not always observed in all measurements. At many gate voltages (typically those with near-zero ΔV_S), the hysteresis was unclear. Nevertheless, applying the aforementioned spin voltage estimation protocol on these data yielded reasonable values of ΔV_S (close to 0). Therefore, the same protocol was applied for all V_G-dependence data.

5. Ruling out the effect of Nb superconductivity

All normal leads of the devices reported in this paper were fabricated using Nb for its good stickiness. However, the spin voltage measurements were performed at the base temperature of the dilution refrigerator (20–40 mK), which is below the superconducting critical temperature T_c of Nb. To confirm that the superconductivity of Nb does not produce any spurious signal that resembles the spin voltage, we performed the spin voltage measurement at 9 K, which is above the T_c of our Nb film (which was approximately 8 K). As shown in Fig. 6, a finite ΔV_S is still observed at 9 K,

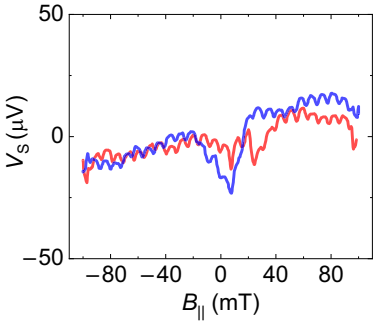

FIG. 6. Voltage hysteresis in device B at 9 K, which is above the T_c of Nb. A finite spin voltage is still discernible in the data.

which confirms that the spin voltage is present irrespective of the superconductivity of Nb.

6. Characterization of materials

The Hall measurement was performed after the spin voltage measurement in each cooldown. Unfortunately, no reliable Hall signal was measured in device A due to bad contacts of the Hall electrodes. The carrier densities estimated from the Hall measurements are shown in Table I. The carrier density in devices B and C was estimated to be in the high 10^{12} cm^{-2} range, which suggests that their chemical potential (at $V_G = 0$ V) was close to the conduction band edge.

7. Reproducibility of the spin transistor effect

A total of three devices are reported in this paper: A, B, and C. While device A showed no sign change in the spin voltage ΔV_S upon gating, device B exhibited a sign change and a complicated oscillation in ΔV_S as a function of V_G. The spin voltage reversal was reproduced in device C: not only was the opposite hysteresis observed between $V_G = 40$ V (TSS origin) and $V_G = -55$ V (Rashba origin), but also the oscillation between plus and minus ΔV_S as a function of V_G was reproduced (see Fig. 7). This reproducibility gives confidence in the intrinsic nature of the spin transistor effect in our TI-based devices.

8. Silicon nitride tunnel barrier

The impedance mismatch between a semiconductor (which is TI in our case) and a FM electrode can strongly hinder the detection of the spin polarization using a FM potentiometer [52]. Therefore, a tunnel barrier between the spin-active material (TI) and the FM is required to compensate for this mismatch [53]. Experimentally, reproducible fabrication of a tunnel barrier with suitable resistance is the main challenge for devices of this type. In this context, Al_2O_3 deposited by atomic layer deposition (ALD) is the material conventionally used for this tunnel barrier due to its high dielectric constant and well-controlled thickness. However, the resistivity of Al_2O_3 deposited by ALD was not reproducible enough in our experiment (we observed a large variation in the tunnel barrier resistance). One possible reason for this irreproducibility is the native oxide on the TI surface that is uncontrolled.

We therefore employed a SiN_x tunnel barrier fabricated by HW CVD. This technique was used because of the low substrate temperature during the deposition [54], in contrast to the high substrate temperature typically associated with the CVD technique. This low substrate temperature makes HW CVD compatible with TI devices, since experiencing a temperature above 120 °C will shift the chemical potential in BSTS [55].

The SiN_x barriers deposited by HW CVD showed more reproducible tunnel-barrier resistances compared to the ALD-prepared Al_2O_3 tunnel barrier.

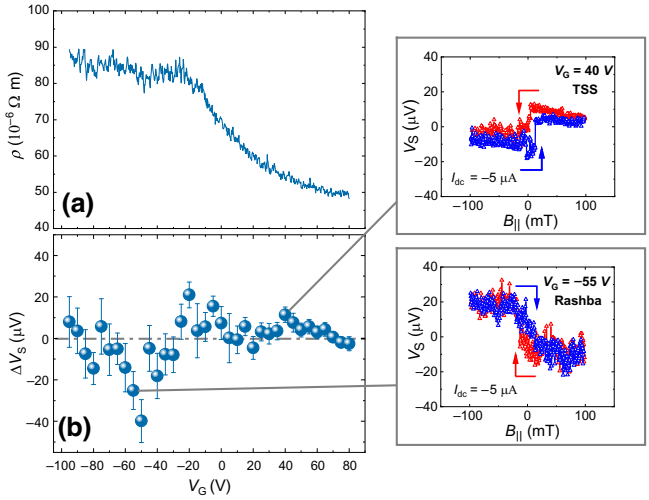

FIG. 7. (a) Resistivity and (b) ΔV_S as a function of V_G measured in device C. Insets: opposite spin polarization hysteresis observed between $V_G = 40$ V and $V_G = -55$ V. In these measurements of device C, the direction of the dc current was opposite to that in the measurements of device B, and hence the V_S vs $B_{||}$ relationship is reversed.

TABLE I. Two-dimensional (2D) carrier density estimated from the Hall measurements at $V_G = 0$ V and the composition of the BSTS crystal used for the device.

Device	A	B	C
2D carrier density (cm^{-2})	...	6.72×10^{12}	9.17×10^{12}
TI composition	$BiSbTeSe_2$	$Bi_{0.5}Sb_{1.5}Te_{1.3}Se_{1.7}$	$Bi_{0.5}Sb_{1.5}Te_{1.3}Se_{1.7}$

9. Calculation of the current-induced spin polarization

First, to connect with the experimental gate voltage dependence of the CISP, we make the simplifying assumption that the capacitance is independent of chemical potential and that the gate voltage changes only the surface density. We obtain this density using Luttinger's theorem, such that

$$n = \frac{k_{F,0}^2}{4\pi} + \sum_{i>0} \frac{(k_{F,i}^{\text{out}})^2 + (k_{F,i}^{\text{in}})^2 \text{sgn}(\mu - \varepsilon_i)}{4\pi} + n_{\text{bulk}}, \tag{A2}$$

where n_{bulk} encodes the fact that in any real experimental setup there is a contribution from bulk impurity states to the density n, which prevents the divergence of the CISP when the chemical potential is at the Dirac point. This equation can be used to obtain $\mu(n)$ because we calculate the CISP (below) for a given chemical potential.

We now derive Eq. (2), namely, the contributions of each individual Fermi pocket [shown in Fig. 3(b)] to the CISP. Using the Boltzmann description [16], we can write the occupation function in the presence of an electric field $\mathcal{E}_x$, to linear order, as

$$f^{(i)}(\mathbf{k}) \approx f_0^{(i)}(\mathbf{k}) + e\tau_i \mathcal{E}_x \frac{\partial f_0^{(i)}(\mathbf{k})}{\partial k_x}.$$

For a given chemical potential the contribution to the spin density of a Fermi surface with helicity $\xi = \pm 1$ is given by

$$n_{\uparrow(\downarrow),i} = \sum_{j\in\{\text{in,out}\}} \frac{1}{8\pi} \left((k_{F,i}^j)^2 + (-)\xi_j k_{F,i}^j e\tau_i \mathcal{E}_x \right), \tag{A3}$$

where the inner and outer Fermi pockets always have opposite helicity (see Fig. 3). Hence the difference in spin density for a single pair of bands i, as appears in the CISP, is given by

$$n_{\uparrow,i} - n_{\downarrow,i} = -e\mathcal{E}_x \frac{\tau_i (k_{F,i}^{\text{out}} - k_{F,i}^{\text{in}})}{4\pi} = \frac{e\mathcal{E}_x}{4\pi} \Delta_i, \tag{A4}$$

where for the topological band $k_{F,i}^{\text{out}} = 0$ because there is only the inner Fermi pocket.

Finally, to calculate the CISP [the result of which is shown in Fig. 2(e)], we need to approximate the transport scattering time, τ_i, for the ith pair of bands. We do this by assuming that only intra-Fermi pocket scattering is relevant, such that the scattering rate is given by

$$\frac{1}{\tau_i} = \gamma \nu_i(\mu) \int \frac{d\theta}{2\pi} (1 - \cos\theta) \cos^2 \frac{\theta}{2} = \frac{\gamma \nu(\mu)}{4}, \tag{A5}$$

where $\nu_i(\mu)$ is the density of states of the given Fermi pocket for the ith band. For the topological Fermi pocket $\nu_0(\mu) = \mu/2\pi\alpha_0^2$, and for the trivial Fermi pocket $\nu_{i\neq 0}(\mu) = m_i/2\pi$. Inserting these scattering times into Δ_i gives the approximations in Eqs. (3) and (4). In reality, interpocket scattering will also occur and this would couple all bands. However, our simple approximation using only intra-pocket scattering is sufficient to capture the change of sign in the CISP observed in our experiment.

10. "Spin transistor"

In this study the term "spin transistor" is used in a slightly different sense than in Ref. [1]. The original proposal of Datta and Das was inspired by optical experiments. It comprises a polarizer (source) and an analyzer (drain) in the form of magnetic contacts on a two-dimensional electron gas (2DEG), in which a spin-polarized current flows. The spin polarization within the 2DEG can be tuned via a gate electrode, based on spin-orbit interaction. As a consequence, the transmission between source and drain can be switched via the application of a gate voltage. The huge interest in spintronics that followed is often motivated by the prospect of realizing low-energy-consumption devices based on spin-dependent phenomena.

Here, we would like to clarify the differences between the Datta-Das transistor and the device in this study. In the Datta-Das transistor, the electric current through the device is controlled by the gate electrode, making it in principle a drop-in replacement for traditional field-effect transistors. Devices like ours, which are based on a TI, instead make use of the fact that a current pushed through the topological surface state intrinsically acquires a spin polarization. Therefore, the FM injector lead working as the polarizer in the Datta-Das transistor is not required. Another difference is that we use the FM lead as a spin polarization detector, not as an analyzer or drain. Note that the output of a spin polarization detector is voltage, whereas the output of an analyzer or drain is electric current. One can understand the present device as a source for a spin-polarized current whose polarization is switchable by gating based on a novel mechanism. This switchability is the crucial ingredient of a spin transistor. In future, the present device design could be modified to include a magnetic drain, turning it into a device similar to the Datta-Das transistor to control the electric current via spin degrees of freedom; the transistor gain can be discussed and evaluated for such a device.

A further difference is that the Datta-Das transistor works, in principle, in the ballistic transport regime, while the present device operates in the diffusive transport regime. This fact may make the application of the present device principle easier.

[1] S. Datta and B. Das, Electronic analog of the electro-optic modulator, Appl. Phys. Lett. **56**, 665 (1990).

[2] I. Žutić, J. Fabian, and S. D. Sarma, Spintronics: Fundamentals and applications, Rev. Mod. Phys. **76**, 323 (2004).

[3] D. D. Awschalom and M. E. Flatté, Challenges for semiconductor spintronics, Nat. Phys. **3**, 153 (2007).

[4] P. Chuang, S.-C. Ho, L. W. Smith, F. Sfigakis, M. Pepper, C.-H. Chen, J.-C. Fan, J. Griffiths, I. Farrer, H. E. Beere, G. A. C. Jones, D. A. Ritchie, and T.-M. Chen, All-electric all-semiconductor spin field-effect transistors, Nat. Nanotechnol. **10**, 35 (2015).

[5] J. Ingla-Aynés, F. Herling, J. Fabian, L. E. Hueso, and F. Casanova, Electrical Control of Valley-Zeeman Spin-Orbit-Coupling–Induced Spin Precession at Room Temperature, Phys. Rev. Lett. **127**, 047202 (2021).

[6] H. C. Koo, J. H. Kwon, J. Eom, J. Chang, S. H. Han, and M. Johnson, Control of spin precession in a spin-injected field effect transistor, Science **325**, 1515 (2009).

[7] C. Li, O. Van't Erve, J. Robinson, Y. Liu, L. Li, and B. Jonker, Electrical detection of charge-current-induced spin polarization due to spin-momentum locking in Bi_2Se_3, Nat. Nanotechnol. **9**, 218 (2014).

[8] Y. Ando, T. Hamasaki, T. Kurokawa, K. Ichiba, F. Yang, M. Novak, S. Sasaki, K. Segawa, Y. Ando, and M. Shiraishi, Electrical detection of the spin polarization due to charge flow in the surface state of the topological insulator $Bi_{1.5}Sb_{0.5}Te_{1.7}Se_{1.3}$, Nano Lett. **14**, 6226 (2014).

[9] J. Tang, L.-T. Chang, X. Kou, K. Murata, E. S. Choi, M. Lang, Y. Fan, Y. Jiang, M. Montazeri, W. Jiang, Y. Wang, L. He, and K. Wang, Electrical detection of spin-polarized surface states conduction in $(Bi_{0.53}Sb_{0.47})_2Te_3$ topological insulator, Nano Lett. **14**, 5423 (2014).

[10] L. Liu, A. Richardella, I. Garate, Y. Zhu, N. Samarth, and C.-T. Chen, Spin-polarized tunneling study of spin-momentum locking in topological insulators, Phys. Rev. B **91**, 235437 (2015).

[11] J. Tian, I. Miotkowski, S. Hong, and Y. P. Chen, Electrical injection and detection of spin-polarized currents in topological insulator Bi_2Te_2Se, Sci. Rep. **5**, 1 (2015).

[12] A. Dankert, J. Geurs, M. V. Kamalakar, S. Charpentier, and S. P. Dash, Room temperature electrical detection of spin polarized currents in topological insulators, Nano Lett. **15**, 7976 (2015).

[13] J. S. Lee, A. Richardella, D. R. Hickey, K. A. Mkhoyan, and N. Samarth, Mapping the chemical potential dependence of current-induced spin polarization in a topological insulator, Phys. Rev. B **92**, 155312 (2015).

[14] F. Yang, S. Ghatak, A. Taskin, K. Segawa, Y. Ando, M. Shiraishi, Y. Kanai, K. Matsumoto, A. Rosch, and Y. Ando, Switching of charge-current-induced spin polarization in the topological insulator $BiSbTeSe_2$, Phys. Rev. B **94**, 075304 (2016).

[15] K. Vaklinova, A. Hoyer, M. Burghard, and K. Kern, Current-induced spin polarization in topological insulator–graphene heterostructures, Nano Lett. **16**, 2595 (2016).

[16] C. H. Li, O. M. van't Erve, S. Rajput, L. Li, and B. T. Jonker, Direct comparison of current-induced spin polarization in topological insulator Bi_2Se_3 and InAs Rashba states, Nat. Commun. **7**, 1 (2016).

[17] P. Li *et al.*, Magnetization switching using topological surface states, Sci. Adv. **5**, eaaw3415 (2019).

[18] Q. L. He, T. L. Hughes, N. P. Armitage, Y. Tokura, and K. L. Wang, Topological spintronics and magnetoelectronics, Nat. Mater. **21**, 15 (2022).

[19] Y. Ando, Topological insulator materials, J. Phys. Soc. Jpn. **82**, 102001 (2013).

[20] S. Bandyopadhyay, Strained topological insulator spin field effect transistor, Mater. Quantum Technol. **3**, 015001 (2023).

[21] V. M. Edelstein, Spin polarization of conduction electrons induced by electric current in two-dimensional asymmetric electron systems, Solid State Commun. **73**, 233 (1990).

[22] A. Aronov and Y. B. Lyanda-Geller, Nuclear electric resonance and orientation of carrier spins by an electric field, Sov. Phys. JETP **50**, 431 (1989).

[23] A. G. Aronov, Y. B. Lyanda-Geller, and G. E. Pikus, Spin polarization of electrons by an electric current, Sov. Phys. JETP **73**, 537 (1991).

[24] Y. Shiomi, K. Nomura, Y. Kajiwara, K. Eto, M. Novak, K. Segawa, Y. Ando, and E. Saitoh, Spin-electricity Conversion Induced by Spin Injection into Topological Insulators, Phys. Rev. Lett. **113**, 196601 (2014).

[25] J. Yu, H. Zhuang, K. Zhu, Y. Chen, Y. Liu, Y. Zhang, C. Yin, S. Cheng, Y. Lai, K. He, and Q. Xue, Observation of current-induced spin polarization in the topological insulator Bi_2Te_3 via circularly polarized photoconductive differential current, Phys. Rev. B **104**, 045428 (2021).

[26] S. M. Hus, X.-G. Zhang, G. D. Nguyen, W. Ko, A. P. Baddorf, Y. P. Chen, and A.-P. Li, Detection of the Spin-Chemical Potential in Topological Insulators Using Spin-Polarized Four-Probe STM, Phys. Rev. Lett. **119**, 137202 (2017).

[27] A. Leis, M. Schleenvoigt, A. R. Jalil, V. Cherepanov, G. Mussler, D. Grützmacher, F. S. Tautz, and B. Voigtländer, Room temperature in-situ measurement of the spin voltage of a $BiSbTe_3$ thin film, Sci. Rep. **10**, 1 (2020).

[28] M. Johnson and R. H. Silsbee, Coupling of electronic charge and spin at a ferromagnetic-paramagnetic metal interface, Phys. Rev. B **37**, 5312 (1988).

[29] J. Tian, C. Şahin, I. Miotkowski, M. E. Flatté, and Y. P. Chen, Opposite current-induced spin polarizations in bulk-metallic Bi_2Se_3 and bulk-insulating Bi_2Te_2Se topological insulator thin flakes, Phys. Rev. B **103**, 035412 (2021).

[30] S. Hong, V. Diep, S. Datta, and Y. P. Chen, Modeling potentiometric measurements in topological insulators including parallel channels, Phys. Rev. B **86**, 085131 (2012).

[31] L. L. Tao and E. Y. Tsymbal, Spin-orbit dependence of anisotropic current-induced spin polarization, Phys. Rev. B **104**, 085438 (2021).

[32] C. H. Li, O. M. van't Erve, C. Yan, L. Li, and B. T. Jonker, Electrical detection of current generated spin in topological insulator surface states: Role of interface resistance, Sci. Rep. **9**, 1 (2019).

[33] J. Schliemann, J. C. Egues, and D. Loss, Nonballistic Spin-Field-Effect Transistor, Phys. Rev. Lett. **90**, 146801 (2003).

[34] J. Schliemann, Ballistic side-jump motion of electrons and holes in semiconductor quantum wells, Phy. Rev. B **75**, 045304 (2007).

[35] G. J. Ferreira, R. P. Maciel, P. H. Penteado, and J. C. Egues, Zitterbewegung and bulk-edge Landau-Zener tunneling in topological insulators, Phy. Rev. B **98**, 165120 (2018).

[36] J. Lan and J. Xiao, Skew scattering and side jump of spin wave across magnetic texture, Phys. Rev. B **103**, 054428 (2021).

[37] Y. Zhang, K. He, C.-Z. Chang, C.-L. Song, L.-L. Wang, X. Chen, J.-F. Jia, Z. Fang, X. Dai, W.-Y. Shan, S.-Q. Shen, Q. Niu, X.-L. Qi, S.-C. Zhang, X.-C. Ma, and Q.-K. Xue, Crossover of the three-dimensional topological insulator Bi_2Se_3 to the two-dimensional limit, Nat. Phys. **6**, 584 (2010).

[38] P. Li and I. Appelbaum, Interpreting current-induced spin polarization in topological insulator surface states, Phys. Rev. B **93**, 220404 (2016).

[39] A. Caviglia, M. Gabay, S. Gariglio, N. Reyren, C. Cancellieri, and J.-M. Triscone, Tunable Rashba Spin-Orbit Interaction at Oxide Interfaces, Phys. Rev. Lett. **104**, 126803 (2010).

[40] V. Fatemi, B. Hunt, H. Steinberg, S. L. Eltinge, F. Mahmood, N. P. Butch, K. Watanabe, T. Taniguchi, N. Gedik, R. C. Ashoori, and P. Jarillo-Herrero, Electrostatic Coupling between Two Surfaces of a Topological Insulator Nanodevice, Phys. Rev. Lett. **113**, 206801 (2014).

[41] M. Bianchi, D. Guan, S. Bao, J. Mi, B. B. Iversen, P. D. King, and P. Hofmann, Coexistence of the topological state and a two-dimensional electron gas on the surface of Bi_2Se_3, Nat. Commun. **1**, 1 (2010).

[42] Z.-H. Zhu, G. Levy, B. Ludbrook, C. Veenstra, J. Rosen, R. Comin, D. Wong, P. Dosanjh, A. Ubaldini, P. Syers, N. P. Butch, J. Paglione, I. S. Elfimov, and A. Damascelli, Rashba Spin-Splitting Control at the Surface of the Topological Insulator Bi_2Se_3, Phys. Rev. Lett. **107**, 186405 (2011).

[43] P. King, R. C. Hatch, M. Bianchi, R. Ovsyannikov, C. Lupulescu, G. Landolt, B. Slomski, J. Dil, D. Guan, and J. Mi *et al.*, Large Tunable Rashba Spin Splitting of a Two-Dimensional Electron Gas in Bi_2Se_3, Phys. Rev. Lett. **107**, 096802 (2011).

[44] M. S. Bahramy, P. D. C. King, A. de la Torre, J. Chang, M. Shi, L. Patthey, G. Balakrishnan, P. Hofmann, R. Arita, N. Nagaosa, and F. Baumberger, Emergent quantum confinement at topological insulator surfaces, Nat. Commun. **3**, 1159 (2012).

[45] J. Wang, C. Gorini, K. Richter, Z. Wang, Y. Ando, and D. Weiss, Two-dimensional-dirac surface states and bulk gap probed via quantum capacitance in a three-dimensional topological insulator, Nano Lett. **20**, 8493 (2020).

[46] V. Iyer, Y. P. Chen, and X. Xu, Ultrafast Surface State Spin-Carrier Dynamics in the Topological Insulator Bi_2Te_2Se, Phys. Rev. Lett. **121**, 026807 (2018).

[47] P. Lazic, K. D. Belashchenko, and I. Zutic, Effective gating and tunable magnetic proximity effects in two-dimensional heterostructures, Phys. Rev. B **93**, 241401 (2016).

[48] J. Xu, S. Singh, J. Katoch, G. Wu, T. Zhu, I. Žutić, and R. K. Kawakami, Spin inversion in graphene spin valves by gate-tunable magnetic proximity effect at one-dimensional contacts, Nat. Commun. **9**, 2869 (2018).

[49] B. Scharf, A. Matos-Abiague, J. E. Han, E. M. Hankiewicz, and I. Zutic, Tunneling Planar Hall Effect in Topological Insulators: Spin Valves and Amplifiers, Phys. Rev. Lett. **117**, 166806 (2016).

[50] C. Shen, T. Leeney, A. Matos-Abiague, B. Scharf, J. E. Han, and I. Zutic, Resonant tunneling anisotropic magnetoresistance induced by magnetic proximity, Phys. Rev. B **102**, 045312 (2020).

[51] P. U. Asshoff, J. L. Sambricio, A. P. Rooney, S. Slizovskiy, A. Mishchenko, A. M. Rakowski, E. W. Hill, A. K. Geim, S. J. Haigh, V. I. Fal'ko, I. J. Vera-Marun, and I. V. Grigorieva, Magnetoresistance of vertical Co-graphene-NiFe junctions controlled by charge transfer and proximity-induced spin splitting in graphene, 2D Mater. **4**, 031004 (2017).

[52] G. Schmidt, D. Ferrand, L. Molenkamp, A. Filip, and B. Van Wees, Fundamental obstacle for electrical spin injection from a ferromagnetic metal into a diffusive semiconductor, Phys. Rev. B **62**, R4790 (2000).

[53] E. Rashba, Theory of electrical spin injection: Tunnel contacts as a solution of the conductivity mismatch problem, Phys. Rev. B **62**, R16267 (2000).

[54] F. Yang, A. A. Taskin, S. Sasaki, K. Segawa, Y. Ohno, K. Matsumoto, and Y. Ando, Top gating of epitaxial $(Bi_{1-x}Sb_x)_2Te_3$ topological insulator thin films, Appl. Phys. Lett. **104**, 161614 (2014).

[55] O. Breunig and Y. Ando, Opportunities in topological insulator devices, Nat. Rev. Phys. **4**, 184 (2022).